The Astrophysical Journal, 588:918–930, 2003 May 10

FIVE STAR-FORMING CORES IN THE GALACTIC RING SURVEY: A MID-INFRARED STUDY

Kathleen E. Kraemer,[1,2,3] James M. Jackson,[2,3] Marc Kassis,[2,3] Lynne K. Deutsch,[2,4] Joseph L. Hora,[3,4] Robert Simon,[2] William F. Hoffmann,[5] G. G. Fazio,[4] Aditya Dayal,[3,6] T. M. Bania,[2] Dan P. Clemens,[2] and Mark H. Heyer[7]

Received 2002 March 4; accepted 2003 January 20

ABSTRACT

We have imaged five dense molecular cores, selected from the Galactic Ring Survey (GRS), in the mid-infrared with the MIRAC3 instrument. We obtained high spatial resolution ($\sim 1''$) images through narrow-band filters at 12.5 and 20.6 μm. Four of the five cores show multiple compact sources, extended structure, or both. Lower resolution observations by the *Infrared Space Observatory* (*ISO*) and the *Midcourse Space Experiment* (*MSX*) suggest that the fifth core is also surrounded by extended emission on large scales ($\gtrsim 2'$). The extended mid-infrared structure is well-correlated with the radio continuum morphology in each of the five cores. This similarity suggests that the hot dust traced by the mid-infrared is located within the H II region, traced by the radio continuum, and not merely in a surrounding photodissociation region or molecular cloud. If a single exciting source is assumed for each core, estimates of the zero-age main-sequence spectral types based on the infrared luminosities are typically 1–2 spectral types earlier than those based on the radio free-free emission. However, allowing for multiple exciting sources and apportioning the far-infrared and radio fluxes to the component sources according to the *mid-infrared* flux distribution produces better agreement between the derived spectral types, with an average difference of less than half a spectral type.

Subject headings: infrared: ISM — stars: formation

1. INTRODUCTION

The properties of young, embedded star clusters are difficult to measure because of the large extinctions of their parental molecular clouds. Observations in the near-infrared (e.g., Straw et al. 1989; Barsony, Schombert, & Kis-Halas 1991; Lada & Lada 1995; Lada et al. 2000) have been successful in determining the properties of many embedded cluster stars, but even at *K* and *L* bands, there can often be significant extinction. Far-infrared (far-IR) studies are useful for determining the total cluster luminosity, but because the angular resolution is typically greater than an arcminute, it has been difficult to resolve the individual stars in deeply embedded clusters. Radio continuum studies can resolve embedded clusters, but because thermal free-free emission arises only from stars with significant Lyman continuum fluxes, the radio studies are limited to stars earlier than B0.

Another problem with the study of embedded clusters is that their distances are often poorly known. Consequently, infrared photometry alone cannot be used to estimate the stellar luminosities or spatial distributions. The distances to the embedded clusters can be determined kinematically if the cluster velocity can be measured. For an embedded cluster, it is easy to measure the velocity of the parental molecular cloud through molecular line spectroscopy at millimeter wavelengths.

Part of our group is undertaking a ^{13}CO $J = 1 \rightarrow 0$ survey of a portion of the Galactic plane. The Boston University–Five College Radio Astronomy Observatory Galactic Ring Survey (GRS) has so far imaged over 30 deg^2 in the Galactic first quadrant. We can use the GRS data to identify star-forming molecular cloud cores and to establish their kinematic distances (e.g., Simon et al. 2001; Jackson et al. 2002).

In this paper we present results from a pilot mid-IR study that has successfully resolved previously confused sources in the far- and mid-IR. With mid-IR flux and morphologies and the distances from the GRS data, we can estimate the total luminosity of the cluster and the proportion contributed by each source. We then compare our derived spectral types with those estimated using the emission at radio wavelength. The mid-IR fluxes are a good measure of the total luminosities contributed by the subcomponents of an embedded cluster.

2. OBSERVATIONS AND DATA REDUCTION

2.1. *MIRAC Data*

We selected five bright molecular cores located in the initial GRS field, near $(l, b) \approx (45^\circ, 0^\circ)$ (Simon et al. 1999): GRSMC 45.073+0.129, GRSMC 45.122+0.132, GRSMC 45.190−0.438, GRSMC 45.453+0.060, and GRSMC 45.478+0.131.[8] Each is associated with an *Infra-*

[1] Air Force Research Laboratory, Space Vehicles Directorate, 29 Randolph Road, Hanscom Air Force Base, MA 01731; kathleen.kraemer@hanscom.af.mil.

[2] Institute for Astrophysical Research, Boston University, Boston, MA 02215; kraemer@bu.edu, jackson@bu.edu, mkassis@bu.edu, deutschl@bu.edu, simonr@chub.bu.edu, bania@bu.edu, clemens@bu.edu.

[3] Visiting Astronomer at the Infrared Telescope Facility, which is operated by the University of Hawaii under contract from the National Aeronautics and Space Administration.

[4] Harvard-Smithsonian Center for Astrophysics, 60 Garden Street, MS 78, Cambridge, MA 02138; ldeutsch@cfa.harvard.edu,jhora@cfa.harvard.edu, gfazio@cfa.harvard.edu.

[5] University of Arizona, Steward Observatory, Tucson, AZ 85721; whoffmann@as.arizona.edu.

[6] IPAC/JPL, Caltech MS 100-22, 770 South Wilson Avenue, Pasadena, CA 91125; adayal@ipac.caltech.edu.

[7] Department of Astronomy, University of Massachusetts, Amherst, MA 01003; heyer@astro.umass.edu.

[8] GRSMC refers to Galactic Ring Survey Molecular Cloud (Simon et al. 2001). For brevity, these will hereafter be referred to as G45.07, G45.12, G45.19, G45.45, and G45.47; newly resolved components will be referred to as G45.xx KJK n.

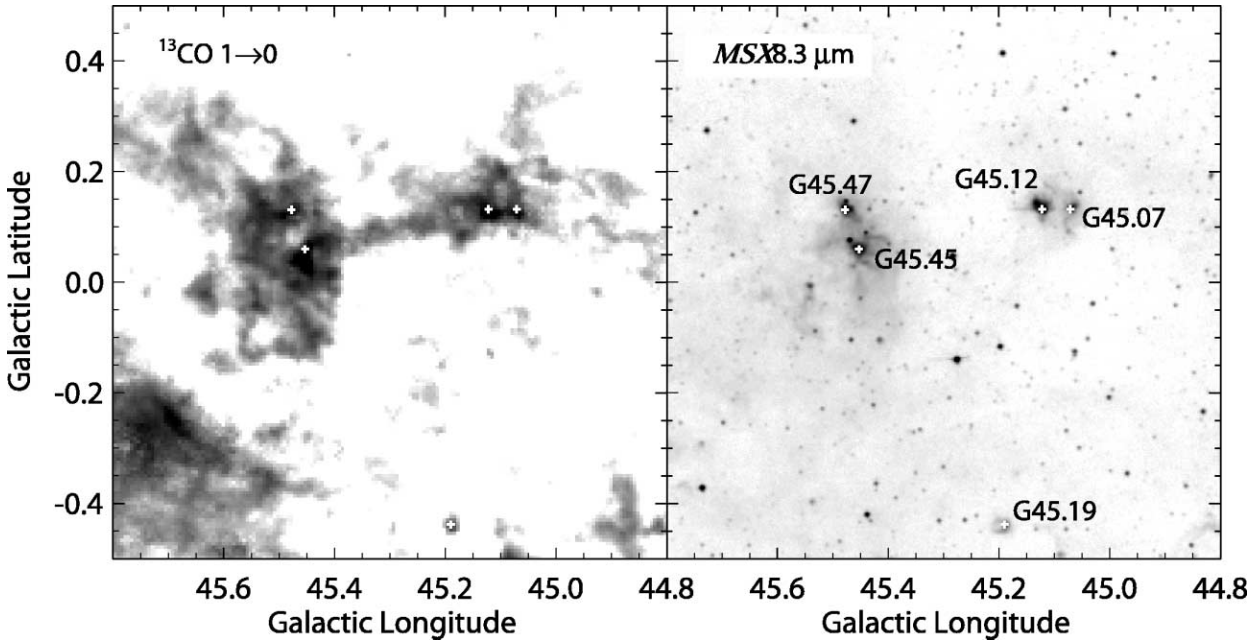

FIG. 1.—*Left:* Integrated intensity image of the ^{13}CO $J = 1 \rightarrow 0$ emission from the Galactic Ring Survey ($10 < I < 100$ K km s^{-1}) integrated from $V_{LSR} = -5$ to $+80$ km s^{-1}. *Right: MSX* Band *A* (~ 8 μm) ($1.9 \times 10^{-6} < I < 4.5 \times 10^{-5}$ W m^{-2} sr^{-1}). Observed cores are marked with plus signs and labeled on the *MSX* image. The gray-scale stretches are logarithmic, where darker is more intense; with these scales, point sources were allowed to saturate in order to highlight the extended emission.

red Astronomical Satellite (*IRAS*) point source (*IRAS* Point-Source Catalog 1988) and with thermal radio continuum emission indicative of H II regions (e.g., Wood & Churchwell 1989; Garay et al. 1993; Testi, Felli, & Taylor 1999; Chaty et al. 2001). Figure 1 shows the GRS ^{13}CO $J = 1 \rightarrow 0$ and *Midcourse Space Experiment* (*MSX*) 8.3 μm images of the region. All five molecular cores show bright ^{13}CO emission and extended (arcminute-scale) mid-IR emission but are unresolved at the resolution of these surveys (45″ for the GRS and 18″ for *MSX*).

The five cores were imaged with the MIRAC3 system (Hoffmann et al. 1998) in 1999 September at the Infrared Telescope Facility (IRTF). MIRAC3 is a ground-based Mid-InfraRed Array Camera built at Steward Observatory (University of Arizona) and Harvard-Smithsonian Center for Astrophysics. An upgrade of the original MIRAC system (Hoffmann et al. 1994), MIRAC3 utilizes a Rockwell HF-16 128 × 128 arsenic-doped silicon, blocked-impurity-band hybrid array operating in a liquid helium-cooled cryostat at 5 K. The telescope was operated in chop-nod mode with a chop frequency of 2 Hz, so the source was in the beam 25% of the time. The infrared standard star γ Aql was used to calibrate the fluxes. Each source was imaged with the 12.5 and 20.6 μm filters, which have bandwidths of 10% and 7%, respectively. Fluxes assumed for γ Aql were 52.1 and 19.7 Jy at 12.5 and 20.6 μm, respectively (see Tokunaga 1984; Rieke, Lebofsky, & Low 1985; Tokunaga et al. 1988; Ball et al. 1992; for details see the MIRAC Users Manual[9] [W. F. Hoffmann & J. L. Hora 1999]). Multiple images with relative offsets of a few arcseconds were taken of each source. Except for G45.47, the images were cross-correlated to the nearest 0.25 pixel and co-added to produce the final maps. Because the emission from G45.47 proved too diffuse and faint to cross-correlate, the nominal telescope offsets were used to register these images. On-source integration times for the final images were ~1–4 minutes per filter (Table 1). The observations were diffraction limited, which corresponds to 1.″1 and 1.″7 at 12.5 and 20.6 μm, respectively, at the IRTF. The plate scale of MIRAC3 at the IRTF is 0.″33 pixel^{-1}.

Point-source sensitivities (noise-equivalent flux density or NEFD) for each co-added field were measured following the procedure described in Kraemer et al. (1999) and are reported in Table 1. For the convolved images used to make the temperature and opacity maps, the standard deviation per pixel was 0.03–0.1 mJy, so the 0.35–1.0 mJy cutoffs (see below) correspond to ~7–14 σ. The fluxes of the mid-IR flux

TABLE 1
OBSERVATIONAL PARAMETERS

Source	Wavelength (μm)	Integration Time (s)	Air Mass	NEFD (mJy)	Observation Date
G45.07.....	12.5	130	1.12	16	1999 Sep 18
	20.6	100	1.14	162	1999 Sep 18
G45.12.....	12.5	100	1.18	24	1999 Sep 18
	20.6	60	1.20	192	1999 Sep 18
G45.19.....	12.5	180	1.01	10	1999 Sep 19
	20.6	220	1.01	67	1999 Sep 19
G45.45.....	12.5	100	1.01	14	1999 Sep 20
	20.6	100	1.01	110	1999 Sep 20
G45.47.....	12.5	180	1.02	10	1999 Sep 20
	20.6	230	1.03	72	1999 Sep 20

NOTE.—Integration times are on-source integration times. NEFDs are 1 σ point-source sensitivities.

[9] Available at http://cfa-www.harvard.edu/~jhora/mirac/mirac.html.

TABLE 2
OBSERVATIONAL AND DERIVED RESULTS

Source	Clump	$F_{12.5}$ (Jy)	$F_{20.6}$ (Jy)	Aperture[a] (arcsec)	$\overline{T}_{12.5/20.6}$ (K)	$\overline{\tau}_{12.5\ \mu m}$
G45.07	KJK 1	35.0	101.6	2.5	140^{+9}_{-8}	$10.3^{+5.2}_{-3.6}$
	KJK 2	13.3	35.2	2.5	154^{+11}_{-10}	$2.4^{+1.2}_{-0.9}$
	KJK 3	2.2	15.7	3.3	110^{+6}_{-5}	$3.7^{+1.9}_{-1.3}$
	Total	65	251	12.0		
G45.12	KJK 1	302	1138	11.0	130^{+8}_{-7}	$7.8^{+4.0}_{-2.7}$
	KJK 2	6.0	48.2	4.0	110^{+6}_{-5}	$8.1^{+4.1}_{-2.8}$
	Total	350	1467	24.0		
G45.19		1.0	4.2	2.0	124 ± 7	$1.1^{+0.5}_{-0.4}$
G45.45	[FSH98] MIR 1	7.4	34.8	3.0	125^{+8}_{-6}	$4.4^{+2.2}_{-1.5}$
	Total	62	321	15.0	125^{+8}_{-6}	$2.4^{+1.2}_{-0.8}$
G45.47	KJK 1	6.8	25.7	8.5	134 ± 8	$0.3^{+0.2}_{-0.1}$
	KJK 2	12.8	27.4	8.5	165^{+13}_{-12}	$0.13^{+0.06}_{-0.05}$

[a] Photometric apertures (diameters) chosen to enclose the maximum flux without overlapping an adjacent aperture. Color temperatures and 12.5 μm opacities are the average value within the given aperture (see text).

calibrators are known to approximately 3% (e.g., Cohen et al. 1995). The mean extinction coefficients were assumed to be 0.125 mag per air mass at 12.5 μm and 0.419 mag per air mass at 20.6 μm, as per Krisciunas et al. (1987). The air masses at which the cores were observed are included in Table 1. Good agreement was found between the fluxes given in the literature (e.g., Felli et al. 2000; Feldt et al. 1998) and in those reported here. The absolute fluxes are estimated to be accurate to better than 10%, with the relative fluxes within a map significantly better than that.

Dust color temperature (12.5/20.6 μm) maps were produced from the ratio of the flux maps under the assumption of blackbody emission modified by a dust emissivity of λ^{-1} (e.g., Scoville & Kwan 1976; Mathis 1990; Dudley & Wynn-Williams 1997; Ghosh & Ojha 2002). Dust opacity maps at 12.5 μm were also produced by comparing the 12.5 μm flux maps with the color temperature maps and solving the standard radiative transfer equation. To increase the signal-to-noise ratio, the flux maps were convolved to 2″ resolution. Flux cutoffs of 0.35–1.0 mJy were applied to the convolved maps prior to the calculations of the color temperature and opacity maps. Fluxes, dust color temperatures, and 12.5 μm dust opacities for each core as a whole, as well as for the individual components, are reported in Table 2. Apertures for the clumps were chosen to enclose the maximum flux without overlapping an adjacent source/aperture. Because of the close spacing and asymmetric nature of the sources, this method probably underestimates the total flux from a given component. Fluxes from the individual clumps will not add up to the "total" flux because of the extended emission present in the larger aperture. Color temperatures and opacities are the mean value within the aperture given in Table 2. If no dust emissivity is included in the calculations, color temperatures increase by ~18% and opacities by a factor of 2.7.

Absolute coordinates shown for each map and listed in Table 3 were determined in the following manner. G45.07, G45.12, and G45.19 each contain at least one compact source detected both in the mid-IR (this work) and in the radio (Garay et al. 1986; Wood & Churchwell 1989; Chaty et al. 2001). The position of the mid-IR source was assumed to correspond to the radio position, and the radio coordinates were adopted. Coordinates for G45.47 were also determined by comparing the mid-IR with the radio emission of Wood & Churchwell (1989), although the lack of well-defined peaks at either radio or mid-IR wavelengths

TABLE 3
SOURCE POSITIONS

Source	Clump	$\Delta\alpha, \Delta\delta$ (arcsec)	R.A. (J2000.0)	Decl. (J2000.0)	Reference
G45.07	KJK 1	0, 0	19 13 22.08	+10 50 53 4	1
	KJK 2	−0.2, +2.0	22.07	55.4	
	KJK 3	−3.8, −4.9	21.82	48.5	
G45.12	KJK 1	0, 0	19 13 27.85	+10 53 36.7	2
	KJK 2	+ 3.8, −6.9	28.10	29.8	
G45.19		0, 0	19 15 39.13	+10 41 17.1	3
G45.45	[FSH98] MIR 1	0, 0	19 14 21.2	+11 04 16	4
G45.47	KJK 1	0, 0	19 14 08.0	+11 12 44	
	KJK 2	+ 11, −18	08.7	26	5

NOTE.—Units of right ascension are hours, minutes, and seconds, and units of declination are degrees, arcminutes, and arcseconds. B1950.0 coordinates from references 1, 2, and 3 were precessed to J2000.0 with the HEASARC Coordinate Converter.

REFERENCES.—(1) Garay et al. 1986; (2) Wood & Churchwell 1989; (3) Chaty et al. 2001; (4) Feldt et al. 1998; (5) Testi et al. 1999.

makes these less reliable. Coordinates for G45.45 are taken from Feldt et al. (1998).

2.2. *Supplementary IRAS Data*

In order to find the luminosity of the clusters forming within the cores, the far-IR fluxes must be determined for each. We obtained *IRAS* data of the initial GRS field from the Infrared Processing and Analysis Center (IPAC). Although the five cores were separated by *IRAS* at 12 and 25 μm, the *IRAS* beam was large enough at 60 and 100 μm that nearby sources were confused. Such source confusion is apparent when two sources have identical fluxes in the *IRAS* Point-Source Catalog (PSC; 1988). For G45.07 and G45.12, which are $\sim 3'$ apart, the PSC gives the fluxes as F_{60} as 5910 Jy and F_{100} as 7500 Jy for both cores. Likewise, at 100 μm, the PSC flux is 7890 Jy for both G45.45 and G45.47, which are $\sim 4\farcm5$ apart. Thus, to better determine the far-IR fluxes associated with the cores, we requested HIRES processing (Aumann, Fowler, & Melnyk 1990) for the field; Figure 2 shows the results of HIRES processing after 20 iterations generated with the default settings.

Point-spread functions (PSFs) were determined using the IDL version of the DAOPHOT procedure *getpsf* on 10–13 stars at each wavelength in the HIRES images. The average values for the FWHMs in the in-scan and cross-scan directions are included in Table 4, and the position angle of 81° was determined from the 12 μm image. Fluxes were integrated within elliptical apertures 1.25 × FWHM, which typically contains 80% of the flux (D. Donovan & D. Clemens 1998, private communication). The HIRES products contained negative fluxes in the background regions ($\sim$35%), therefore no background fluxes were subtracted. Because even the HIRES-processed PSFs are larger than the regions imaged with MIRAC and the region has significant extended mid-IR emission, the fluxes given in Table 4 should be considered upper limits, especially at 60 and 100 μm.

3. RESULTS

Figures 3, 4, 5, and 6 show the four molecular cores with multiple emission sources and extended structure on scales

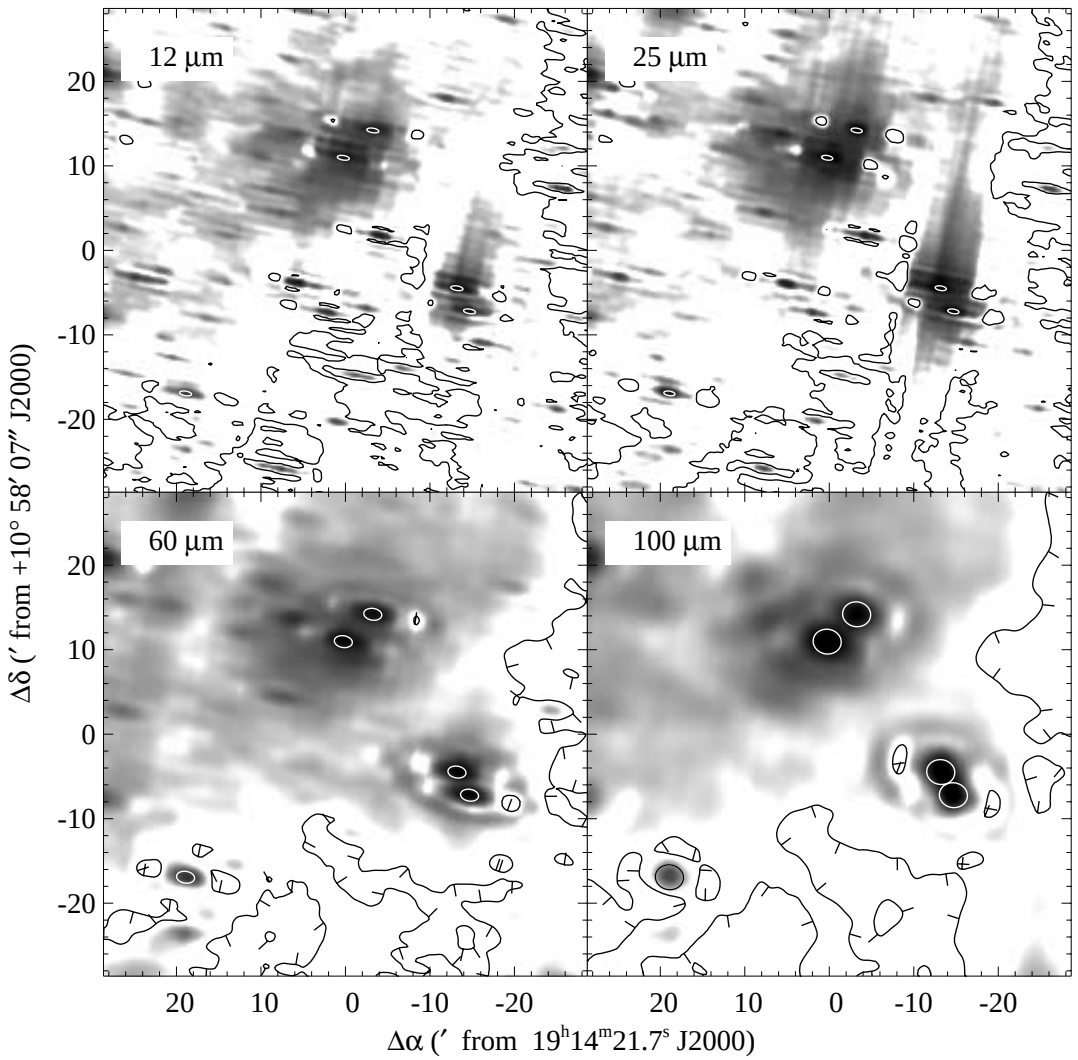

FIG. 2.—HIRES-processed *IRAS* images after 20 iterations. *Upper left:* At 12 μm, $5 < I < 10^4$ MJy sr^{-1}; *upper right:* at 25 μm, $5 < I < 10^4$ MJy sr^{-1}; *lower left:* at 60 μm, $25 < I < 10^4$ MJy sr^{-1}; and *lower right:* at 100 μm, $10^2 < I < 10^4$ MJy sr^{-1}. Ellipses show the areas over which the images were integrated to obtain fluxes, as explained in the text. Data inside the contours have negative values, indicated by the tick marks in the 60 and 100 μm images. Ringing artifacts from the HIRES processing can be seen around the bright cores, especially at 60 and 100 μm.

TABLE 4
IRAS AND HIRES FLUXES

λ (um)	Aperture (arcmin^2)	Flux (Jy)				
		G45.07	G45.12	G45.19	G45.45	G45.47
12.....	PSC	58	250	7	79	37
	Ap1 1.4 × 0.5	39	208	4	45	23
25.....	PSC	494	1400	34	640	304
	Ap1 1.3 × 0.5	327	742	19	357	201
60.....	PSC	5910	5910	277	5340	2610
	Ap1 2.2 × 1.4	3336	5029	202	3903	2091
100.....	PSC	7500	7500	489	7890	7890
	Ap1 3.3 × 2.9	4488	6408	416	6801	3671

NOTE.—Aperture 1 is based on the PSF of point sources in the HIRES 20th iteration images. In the Extended Source Catalog, the fluxes for G45.07/12 are 12,500 and 14,300 Jy at 60 and 100 μm, respectively, and 16,000 Jy for G45.45/47 at 100 μm.

of ~5″–20″: G45.07, G45.12, G45.45, and G45.47. In contrast, G45.19, in Figure 7, shows only a single, compact object on these scales, although it does show extended mid-IR emission on larger (arcminute) scales (Felli et al. 2000; Chaty et al. 2001). Table 3 summarizes the source positions within each core. (The distance adopted is the kinematic distance $d_k = 6$ kpc [Simon et al. 2001], so 1′ corresponds to 1.75 pc.)

3.1. *Individual Sources*

3.1.1. *G45.07*

G45.07, coincident with IRAS 19110+1045, contains three compact components in the mid-IR: G45.07 KJK 1, 2, and 3 (Fig. 4). Two of these components, KJK 1 and 3, had previously been detected in the radio (Garay et al. 1986). The brightest component, KJK 1, contributes roughly half of the total flux at both 12.5 and 20.6 μm. The newly discovered component, KJK 2, is the second brightest and

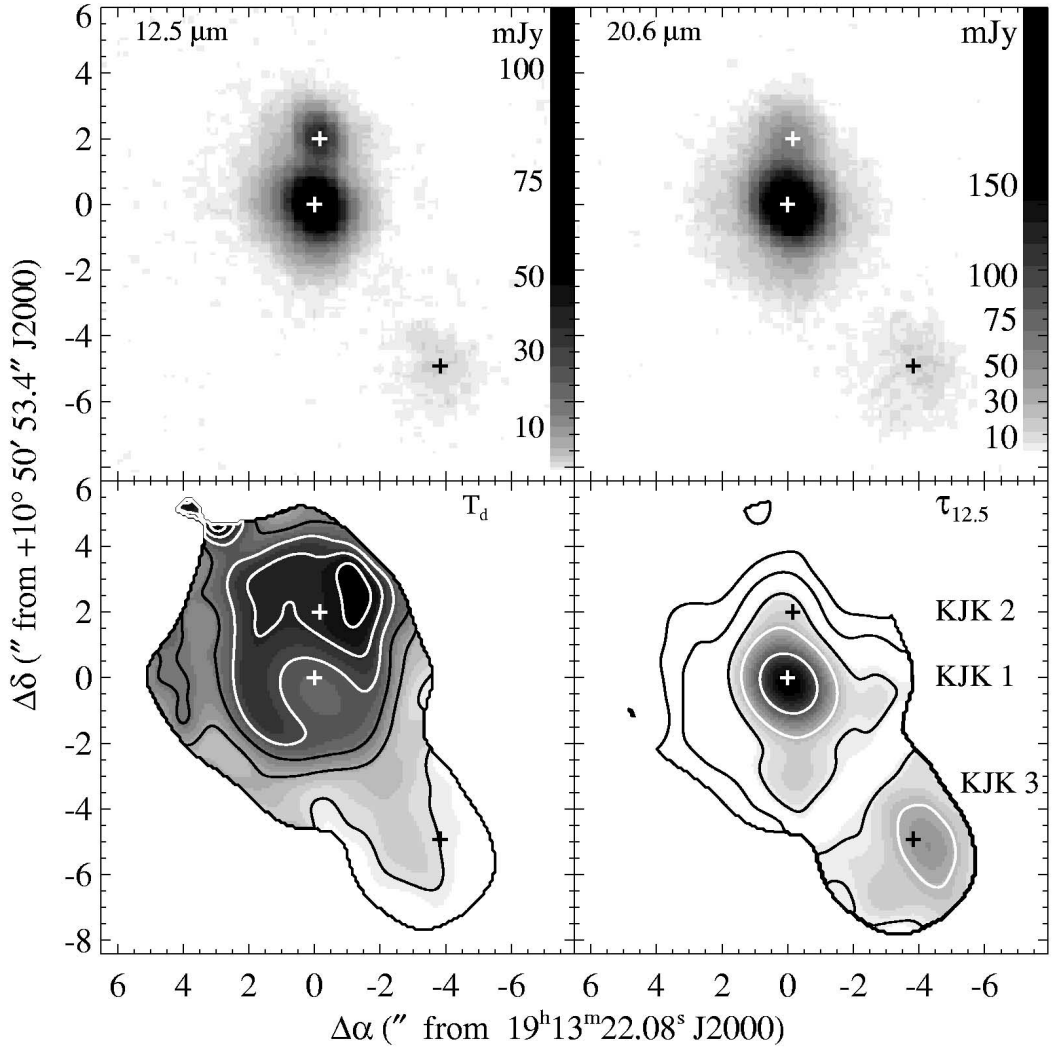

FIG. 3.—Mid-IR emission from G45.07. Three compact mid-IR components are detected at both 12.5 (*upper left*; $0.6 < F < 39$ mJy pixel^{-1}) and 20.6 μm (*upper right*; $4.4 < F < 158$ mJy pixel^{-1}). Color temperature (*lower left*; $105 < T_d < 165$ K, contours at 100, 110, 120, 130, 140, and 150 K), and opacity (*lower right*; $1.4 < \tau_{12.5} < 160 \times 10^{-3}$, contours at 0.5, 1.0, 2.0, 4.0, and 10.0×10^{-3}) maps are also shown. To better show the extended emission, G45.07 KJK 1 and 2 are saturated in the 12.5 μm image and KJK 1 in the 20.6 μm image. (The ringlike structure centered on KJK 1 in the temperature map is an artifact due to the beam-matching process.) In Figs. 4–7, darker is brighter, hotter, or more opaque, as appropriate; flux and opacity gray scales are logarithmic; cores may be saturated to show the extended emission; and compact mid-IR sources are indicated with pluses and labeled in the opacity maps.

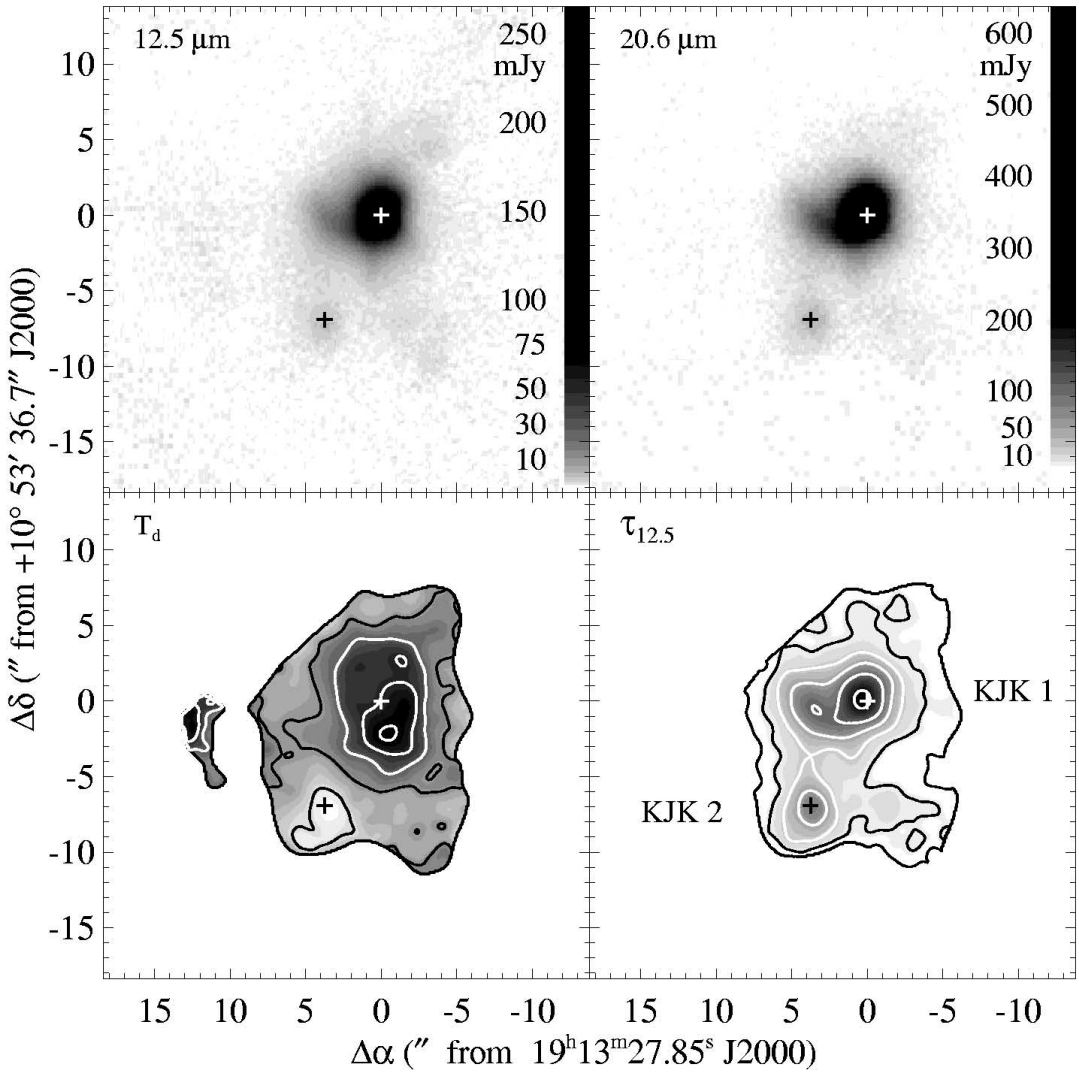

FIG. 4.—Mid-IR emission from G45.12. The core emission dominates the images at both 12.5 (*upper left*; $0.4 < F < 80$ mJy pixel^{-1}) and 20.6 μm (*upper right*; $4 < F < 218$ mJy pixel^{-1}). Color temperature (*lower left*; $105 < T_d < 150$ K, contours at 110, 120, 130, 140, and 150 K) and opacity (*lower right*; $4.5 < \tau_{12.5} < 160 \times 10^{-3}$, contours at 1.25, 2.5, 5.0, 10.0, 20.0, 40.0×10^{-3}) maps are also shown. KJK 1 is saturated in both flux maps to better show the extended emission.

lies just 2″ north of the main peak. The third component, KJK 3, lies ~5″ southwest and is associated with the 2 cm source dubbed G45.07+0.13A by Garay et al. (1986). Based on radial profiles, G45.07+0.13A is slightly extended at both mid-IR and radio wavelengths (Garay et al. 1986; this work). The other two mid-IR components are unresolved sources surrounded by a fainter extended envelope at both 12.5 and 20.6 μm. (The slight elongation northeast-southwest in the compact mid-IR sources is also seen in the trailing γ Aql observation and thus is problematic.)

3.1.2. *G45.12*

G45.12, coincident with IRAS 19111+1048, consists of a main core, G45.12 KJK 1, responsible for ~83% of the flux, surrounded by an extended envelope (Fig. 5). An arc of emission extends from the core toward the east, and a separate component is detected in the southeast. This second mid-IR peak, KJK 2, corresponds to an opacity peak and temperature minimum in the opacity and color temperature maps. The extended arc, while a strong feature in the opacity map, does not stand out in the temperature map.

The detailed correspondence of the mid-IR emission with the radio continuum emission is particularly good in G45.12 (see § 4.1). As in the mid-IR, the radio emission from G45.12 is dominated by a single, bright core surrounded by extended emission (Hofner, Peterson, & Cesaroni 1999; Testi et al. 1999). The two local maxima south of the core found by Hofner et al. (1999) at 1.3 cm are also detected at 12.5 and 20.6 μm. There is also an extension of the 12.5 μm emission to the northwest, in the direction of the third 1.3 cm local maximum (Hofner et al. 1999). The mid-IR tail to the east, which gives this source a slightly "paisley" appearance, correlates well with the higher resolution (0.″4) 2 and 6 cm images of Wood & Churchwell (1989). Given this correspondence over a range of scales from ~1″ to $\gtrsim$20″, the statement of Hayward et al. (1994) that the mid-IR emission and radio emission for this source look "quite different" is somewhat surprising. The presence of spectral features, such as the 11.2 μm UIR (unidentified infrared, usually attributed to polycyclic aromatic hydrocarbons or PAHs) emission feature in their bandpass ($\lambda = 11.7$ μm, $\Delta\lambda \sim 1.1$ μm; Hayward et al. 1993) or the 12.8 μm Ne II line in

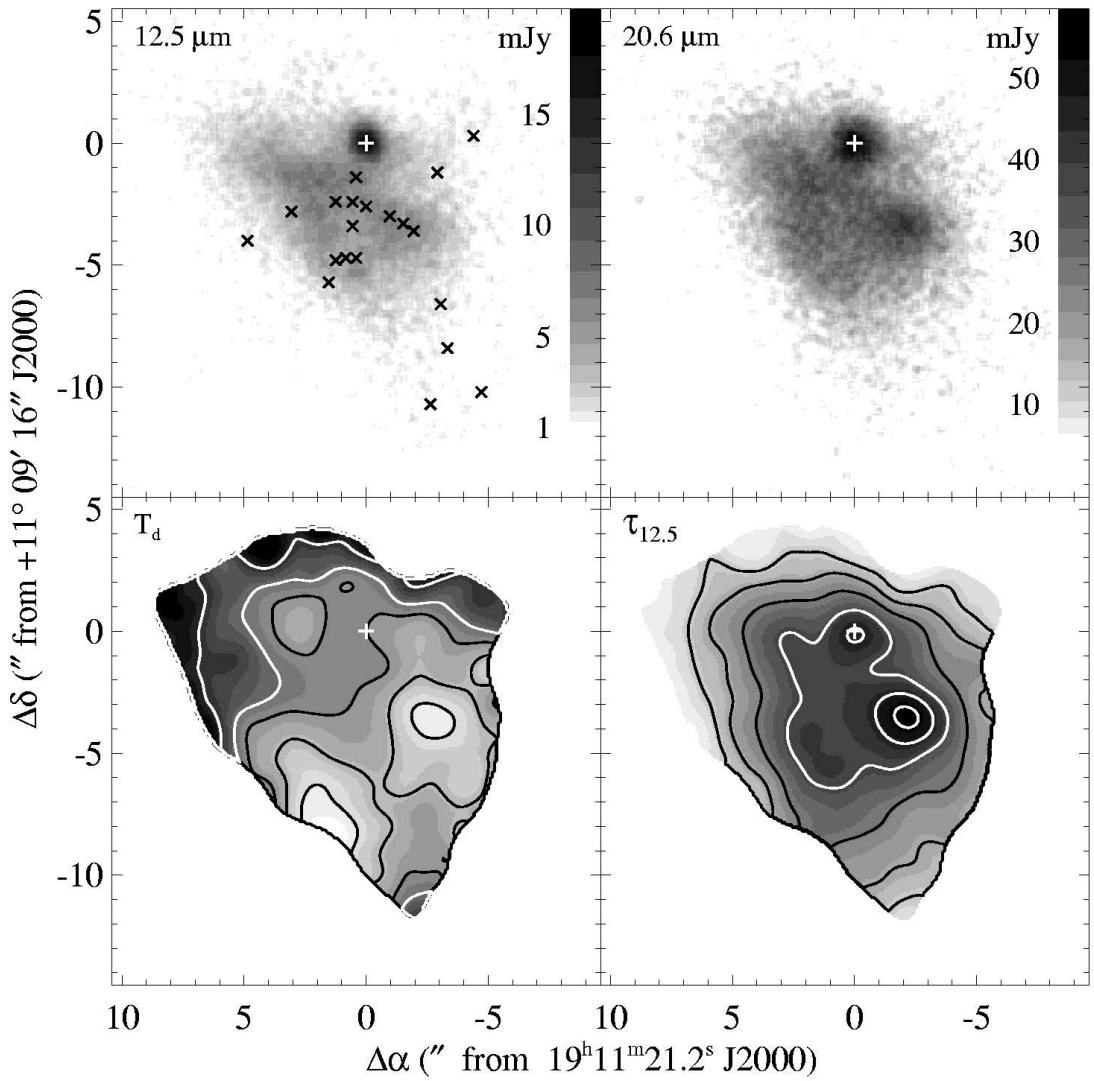

FIG. 5.—Mid-IR emission from G45.45. The compact component [FSH98] MIR 1 contributes roughly 10% of the flux at both 12.5 (*upper left*; $1 < F < 20$ mJy pixel^{-1}) and 20.6 μm (*upper right*; $6 < F < 58$ mJy pixel^{-1}). Color temperature (*lower left*; $110 < T_d < 150$ K, contours at 110, 115, 120, 125, 130, and 140 K) and opacity (*lower right*; $0.1 < \tau_{12.5} < 17.8 \times 10^{-3}$, contours at 0.5, 1, 2, 4, 6, and 8×10^{-3}) maps are also shown. Asterisks in the 12.5 μm map show the positions of the near-IR sources found by Feldt et al. (1998).

the MIRAC3 bandpass ($\lambda = 12.5$ μm, $\Delta\lambda = 1.25$ μm), might explain the discrepancy, although spectroscopic observations are needed to test this.

3.1.3. *G45.19*

G45.19, IRAS 19132+1035, the weakest and most isolated of the ^{13}CO cores observed, is similarly uncomplicated in the mid-IR from ground-based observations (Fig. 3). A single compact component is detected at 12.5 and 20.6 μm, with no extended emission detected on scales less than $\sim$0.′5. Only on larger scales, 1′–2′, with space-based instruments such as *MSX* (Fig. 1) or *Infrared Space Observatory* (*ISO*) (Felli et al. 2000), is extended IR emission detected from G45.19.

3.1.4. *G45.45*

G45.45, IRAS 19120+1103, consists of the bright compact source [FSH98] MIR 1 (Feldt et al. 1998) plus extended mid-IR emission to the southeast (Fig. 6). The second compact mid-IR source noted by Feldt et al. (1998), [FSH98] MIR 2, is tentatively detected at 12.5 μm at (+0.″4, −5.″2) but does not stand out above the extended emission at 20.6 μm.

The extended emission is associated with a dozen near-IR point sources as well as Brγ emission (Feldt et al. 1998) and radio continuum emission (Wood & Churchwell 1989; Garay et al. 1993). Although it contributes more than 10% of the flux at 12.5 and 20.6 μm, [FSH98] MIR 1 does not have a strong radio counterpart (Wood & Churchwell 1989; Hofner et al. 1999). The relative weakness of the radio emission from [FSH98] MIR 1, only recently detected by Hofner et al. (1999), the warm, opaque dust, and the large IR luminosity suggest the presence of a very young, deeply embedded object. Three of the near-IR sources, *h, i*, and *k*, correspond to the peak of the 12.5 μm opacity distribution as well as a peak in the radio continuum map (Wood & Churchwell 1989; Feldt et al. 1998). This position is also a minimum in the color temperature map and is near a local maximum in the 2.2 μm extinction calculated by Feldt et al. (1998). Three other near-IR sources, *l*, *m*, and *o*, surround [FSH98] MIR 2, a compact radio source and another (weak)

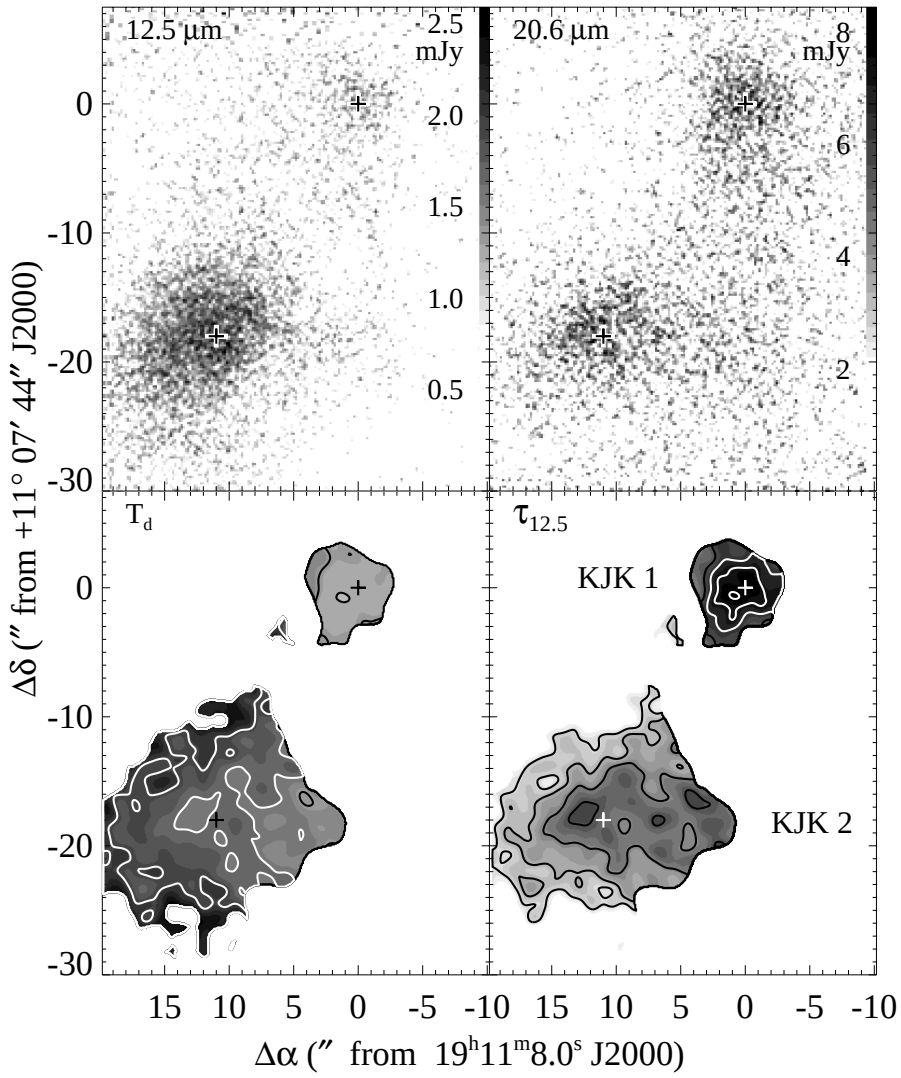

FIG. 6.—Mid-IR emission from G45.47. The core emission dominates the images at both 12.5 (*upper left*; $1 < F < 3$ mJy pixel^{-1}) and 20.6 μm (*upper right*; $2 < F < 8$ mJy pixel^{-1}). Color temperature (*lower left*; $105 < T_d < 285$ K, contours at 130, 140, 160, and 190 K) and opacity (*lower right*; $0.1 < \tau_{12.5} < 5.1 \times 10^{-4}$, contours at 0.25, 0.5, 1.0, 2.0, 3.0, 4.0, and 5.0×10^{-4}) maps are also shown.

opacity enhancement and temperature trough. The latter three are probably less embedded than the former three, all of which are more evolved than [FSH98] MIR 1. No compact source is detected at the position of the eastern radio point source that coincides with *a*, although a compact source with $F(12.5\ \mu\text{m}) < 0.9$ Jy and $F(20.6\ \mu\text{m}) < 4.4$ Jy could be masked by the extended envelope.

3.1.5. *G45.47*

G45.47, associated with IRAS 19117+1107, is the only source in the sample with no compact sources. Instead, it consists of two regions of diffuse emission and no coherent internal structure, similar to the structureless radio continuum emission (Garay et al. 1993; Testi et al. 1999). The northern component corresponds to the peak in the opacity map and is ~30 K colder than the southern component. The east-west elongation detected in the southern component corresponds to a similar elongation observed at radio wavelengths (Garay et al. 1993; Testi et al. 1999).

4. DISCUSSION

4.1. *Mid-IR and Radio Morphologies*

The distribution of the mid-IR emission in the five cores is generally well-correlated with the radio-continuum emission (Garay et al. 1986; Feldt et al. 1998; Testi et al. 1999), especially the extended emission. Figures 8 and 9 show the radio-continuum emission compared to the mid-IR continuum emission for G45.12 and G45.47 (see also Fig. 6 of Chaty et al. 2001, for G45.19). The measured dust color temperatures can help constrain the location of emitting dust with respect to the H II region. The good morphological correlation between the radio and mid-IR emission in the GRS sources suggests that the hot dust is either within the H II region itself or in a thin shell around the H II region. The mean 12.5/20.6 color temperatures are $\overline{T}_d \approx 110$–165 K (Table 2). In models of spherical dust cocoons outside the H II regions around O stars (Churchwell, Wolfire, & Wood 1990), this temperature range only occurs in a narrow shell with radius $r \sim (1\text{–}2) \times 10^{17}$ cm from the central O6 star

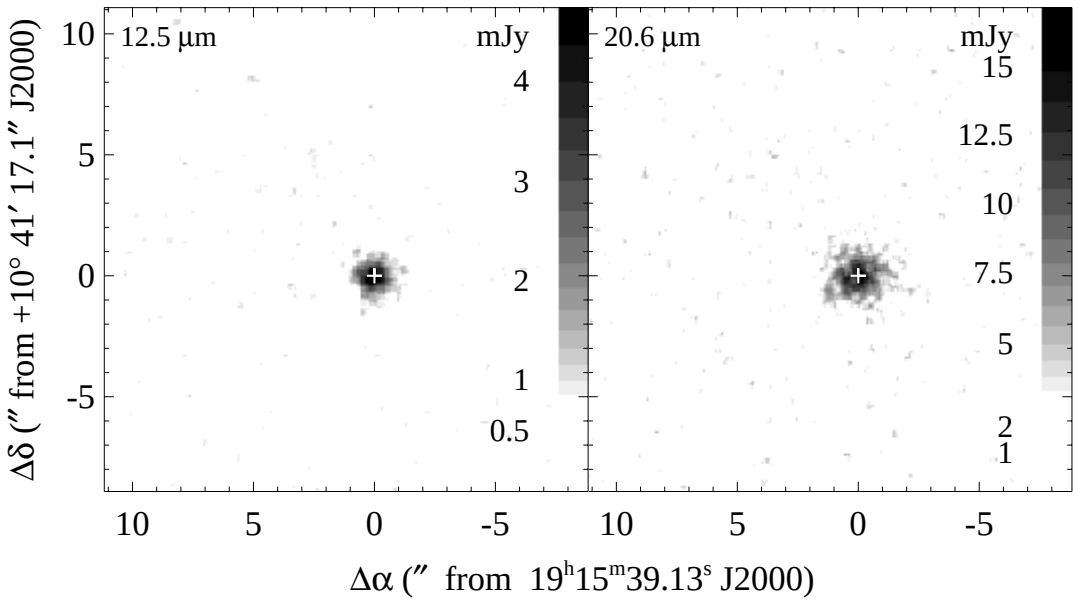

FIG. 7.—Mid-IR emission from G45.19: 12.5 μm (*left*; $0.8 < F < 5.6$ mJy pixel^{-1}) and 20.6 μm (*right*; $3 < F < 16$ mJy pixel^{-1})

because the dust temperature drops so steeply with radius. For models in which the dust is within the H II region (e.g., Natta & Panagia 1976), dust at the observed temperatures also occur in shells in the outer parts of the H II region. However, none of the cores observed here show evidence for limb-brightened dust emission, such as that seen in Mon R2 (e.g., Hackwell, Grasdalen, & Gehrz 1982; Kraemer et al. 2001), which would be expected if the dust were in an optically thin shell in or around the ionized gas. If the gas and dust within the H II region is sufficiently clumpy, though, the observed dust temperatures could occur throughout the H II region. The mid-IR emission would trace the ionized gas without limb brightening, as appears to be the case in the five cores.

4.2. *Evolutionary Status?*

The four cores with multiple sources and extended structure are part of the same larger molecular cloud complex, GRSMC 45.46+0.05 (Simon et al. 2001). Looking across

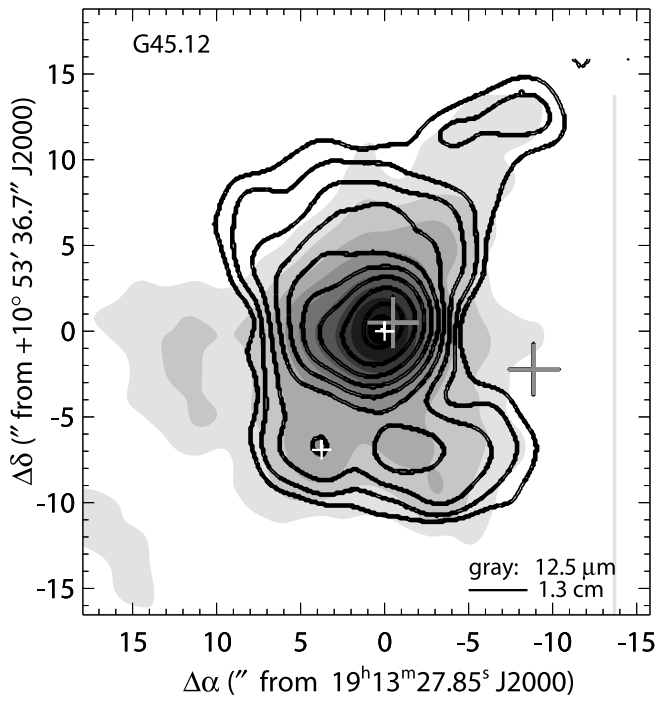

FIG. 8.—12.5 μm emission from G45.12 (*gray scale*, smoothed to 2″) vs. 1.3 cm radio continuum emission (*contours*, ~2.″5 beam; adapted from Fig. 1 of Hofner et al. 1999). The small white pluses are the mid-IR sources discussed in the text; the large black pluses are the outflow centers found by Hunter, Peterson, & Cesaroni (1997).

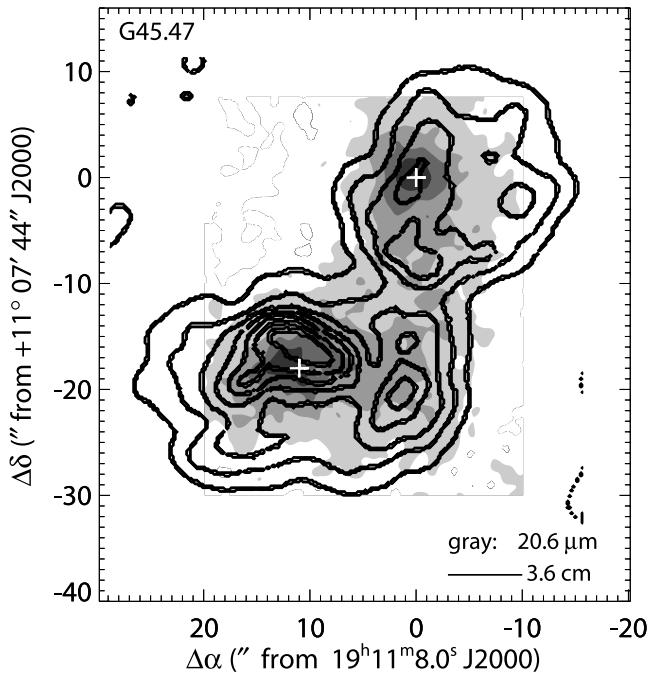

FIG. 9.—20.6 μm emission from G45.47 (*gray scale*, smoothed to 2″) vs. 3.6 cm radio continuum emission (*contours*, adapted from Fig. A5 of Testi et al. 1999). The pluses are the mid-IR positions discussed in the text.

the complex, the nature of compact sources and extended emission from the cores changes from west to east. The westernmost core, G45.07, contains three compact sources and very little extended emission. Slightly farther east, G45.12 contains two compact sources plus extended emission. G45.45 has only one compact source with significant extended emission. Farthest east, G45.47 has only extended emission with no compact sources. Since the dust appears to be well-mixed in the H II regions (§ 4.1), the mid-IR morphologies could reflect the progression of star formation activity in the cloud complex. If the ionization fronts of the different H II regions are advancing into material of comparable density, then the size of each ionized region (traced by the dust as well as by the radio emission) is related to length of time it has been expanding (e.g., Dyson & Williams 1997). Thus, G45.47, with only extended emission, would be the most evolved of the H II regions, while G45.07, with only compact sources, would be the youngest. An alternative explanation is that the gas density changes greatly from core to core. The CS 2→1 emission is brighter toward the western cores (McQuinn et al. 2002), which could indicate denser gas confining the H II regions. Observations of additional molecular gas transitions are needed to determine the molecular gas properties before these two scenarios can be distinguished.[10] (The fifth core, G45.19, is at a slightly higher velocity, and while still at the tangent point, is probably not in the same cloud complex.)

4.3. *IR and Radio Spectral Types*

Studies that have compared radio-derived spectral types with those derived from far-IR observations, from the KAO or balloon-borne experiments as well as from *IRAS*, often find far-IR luminosities that imply spectral types 1–2 types earlier than those derived from the radio continuum flux (e.g., Harvey & Gatley 1983; Wood & Churchwell 1989). Direct comparisons can be difficult because the far-IR luminosities are typically derived from observations with a large beam, in which the structure evident in the higher resolution radio data is unresolved. Also, diffuse radio emission may be "resolved out" in interferometric observations, resulting in an underestimate of the radio flux relative to that detected in the large far-IR beam.

Since an important goal of the GRS project is to compare the luminosity function of star-forming regions in the molecular ring to theoretical luminosity functions, understanding the complexity of the sources, including source multiplicity, is key. Instead of assigning all the radio or far-IR flux to a single source, an accurate estimate of the luminosity function must include multiple sources. Here based on the good correspondence between the mid-IR and radio morphologies in the GRS cores, we examine a method for apportioning those fluxes among several components.

Two methods are considered for determining infrared spectral types from *IRAS* fluxes, that of Helou et al. (1988) and of Emerson (1988). Following Helou et al. (1988), the total flux integrated from 1 to 1000 μm is

$$F_{\rm H} = 1.26 \times 10^{-14} a(2.58F_{60} + F_{100})\ ({\rm W\ m^{-2}})\ , \quad (1)$$

where F_{60} and F_{100} are the fluxes in Jy. The conversion factor a depends on the 60 μm /100 μm flux ratio and is $a \sim 1.4$–1.6 (see Table 3 of Helou et al. 1988) for a dust emissivity index of $n = 1$, in their nomenclature. From Emerson (1988), the integrated flux from 7 to 135 μm is

$$F_{\rm E} = 10^{-14}(20.653F_{12} + 7.538F_{25} + 4.578F_{60} + 1.762F_{100})\ ({\rm W\ m^{-2}})\ . \quad (2)$$

The luminosity is then

$$L = 4\pi d_k^2 F({\rm W}) \quad (3a)$$

$$\approx 1.108 \times 10^{15} F\ (L_\odot)\ , \quad (3b)$$

where the distance is the kinematic distance $d_k = 6$ kpc (Simon et al. 2001). The zero-age main-sequence (ZAMS) spectral type can then be found using Table 1 of Panagia (1973). Use of the Emerson (1988) formula results in spectral types that are no more than 0.5 types earlier than those found with the Helou et al. (1988) formula, and they are usually identical. Since the results are so similar, only the luminosities and ZAMS spectral types determined by the Emerson method are included in Table 5.

[10] See M. Brüll, C. Kramer, & J. Stutski 2000, "CO Multiline Observations near the Galactic 5 kpc Ring with KOSMA" (abstracted in ADS).

TABLE 5
IR and Radio Spectral Types

Source	Flux Fraction (%)	log$L_{\rm IR}$ ($L_\odot$)	ZAMS IR	$F_{\rm radio}$ (Jy)	u (pc cm^{-2})	ZAMS Radio
G45.07 total		5.47	O6	0.27	29.23	O9
KJK 1	53	5.19	O6.5	0.33	31.71	O9
KJK 2	20	4.77	O8.5–8	...	...	<B0
KJK 3	3	3.94	B0.5	0.11	21.84	B0–O9.5
G45.12 total		5.69	O5	3.30	68.54	O6
KJK 1	86	5.62	O5	2.56	63.09	O6
KJK 2	2	3.92	B0.5	0.07	18.60	B0
G45.19		4.32	B0	0.07	18.96	B0
G45.45 total		5.57	O5.5	1.1	46.82	O7
[FSH98] MIR 1	12	4.64	O9	0.13	23.09	O9.5
G45.47 total		5.30	O6.5–6	1.5	52.73	O6.5
KJK 1	35	4.84	O8	0.35	32.08	O8.5
KJK 2	65	5.12	O6.5	1.16	48.33	O7

NOTE.—Radio continuum data are 3.6 cm fluxes from Testi et al. 1999.

Next, the *IRAS* HIRES fluxes from Table 4 are divided among the components in each core based on the ratios of the MIRAC 12.5 μm fluxes relative to the total flux from the core. For example, for G45.12, the brightest component is 86% of the total at 12.5 μm (Table 2), the second component contributes $\sim$2% of the flux, and the remaining flux presumably arises from the sources responsible for the extended emission. In G45.07, the three detected components account for only 69% of the total flux. If the remaining 31% of the flux (outside the chosen apertures) should be attributed to the three known sources, their spectral types would be $\lesssim$0.5 subclasses earlier. The remaining flux could also come from a cluster of lower mass stars below our point-source sensitivity.

Use of the 20.6 μm flux ratios or the *IRAS* 12 or 25 μm fluxes or an average of these values, instead of the 12.5 μm flux ratios, to divide the *IRAS* HIRES fluxes produces ZAMS that differ by less than 0.5 subclasses in most cases. Only the two components in G45.47 have significantly different flux ratios at 12.5 and 20.6 μm: $\sim$2 : 1 and $\sim$1 : 1 at 12.5 and 20.6 μm, respectively. ZAMS spectral types were calculated using 20.6 μm ratio to apportion the *IRAS* HIRES fluxes, which results in O7 for both components, as opposed to O8 and O6.5 with the 12.5 μm flux ratio. While this method of dividing the flux does not properly treat the underlying spectral energy distributions (SEDs) of the sources, it simplifies the calculations considerably and has little effect on the results.

Many radio continuum observations of the GRS dense cores resolved them into multiple components. However, the integrated fluxes, and hence estimates of the ZAMS spectral types, are typically given for the entire region (e.g., Wood & Churchwell 1989; Hofner et al. 1999). Therefore, as with the IR fluxes, we assign a portion of the radio-continuum flux to each component detected in the mid-IR, with the radio flux divided among the components in the same ratio as their mid-IR flux. The strong similarity between the radio and mid-IR emission supports the application of this method to the radio flux as well as to the *IRAS* fluxes. The 3.6 cm fluxes of Testi et al. (1999)[11] and the models of Panagia (1973, his Table 2) are used to estimate the ZAMS for each component by calculating the excitation parameter following the formulation of Schraml & Mezger (1969):

$$u = 4.5526\left[a^{-1}\left(\frac{\nu}{\mathrm{GHz}}\right)^{0.1}\left(\frac{T_e}{\mathrm{K}}\right)^{0.35}\left(\frac{S}{\mathrm{Jy}}\right)\left(\frac{D}{\mathrm{kpc}}\right)^{2}\right]^{1/3} \quad (4a)$$

$$\approx 46.06\left(\frac{S}{\mathrm{Jy}}\right)^{1/3}. \quad (4b)$$

The frequency ν is 8.5 GHz, the distance is the kinematic distance $d_k = 6$ kpc, the electron temperature is $T_e = 8000$ K, a is approximately 1, and S is the integrated flux density. The radio results are included in Table 2.

Figure 10 shows a comparison of the IR and radio ZAMS spectral types calculated with our method as well as those calculated assuming that the emission in each core arises from a single source. The spectral types are also given in Table 2. In most cases, the two spectral types from our method are within 0.5 subclasses for each component in the cores (mean difference = 0.48 subclasses). In contrast, the assumption of a single source in each of the four multicomponent cores leads to a far-IR spectral type earlier than that from the radio flux by more than one subclass. (Use of the PSC fluxes without HIRES processing leads to similar results.) Two lines are plotted in the figure: one that shows a linear fit to the ZAMS spectral types from our method and one that shows the locus where the radio and IR ZAMS spectral types are equal. If the uncertainties in the spectral type determinations are of order 0.5 subclasses (the size of the error bars in the figure), the difference between the two lines is statistically insignificant. The improved agreement over the single-source assumption implies that although our method for apportioning the *IRAS* and radio fluxes among the sources is admittedly coarse, it provides good results.

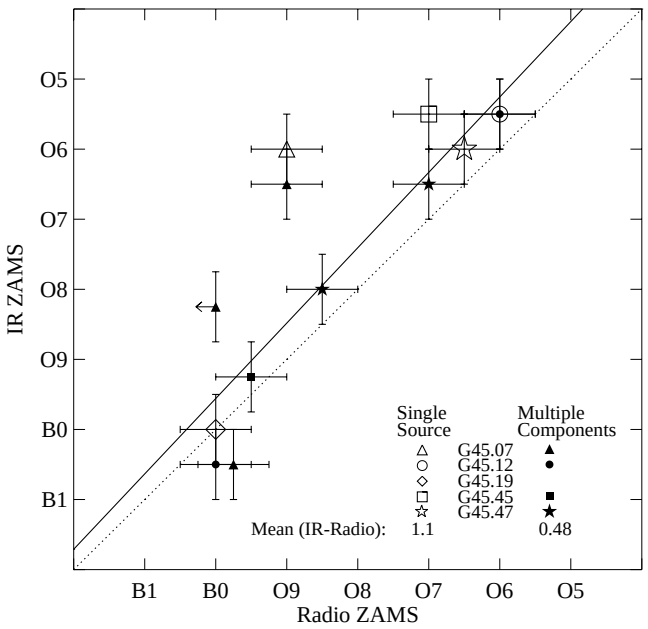

FIG. 10.—ZAMS spectral type estimates from IR data vs. those from radio data for the five observed cores. Estimates using the flux apportionment method described in the text are shown with filled symbols. Estimates assuming a single source produces all the flux are shown with open symbols. The solid line is a linear fit to the spectral types from our apportionment method; the dotted line shows the locus where the radio and IR ZAMS spectral types are equal. Error bars are $\pm$0.5 spectral classes.

The idea that multiple components or star clusters could resolve this discrepancy seen in many sources is certainly not new (e.g., Wood & Churchwell 1989; Kurtz, Churchwell, & Wood 1994). However, the use of high-resolution mid-IR observations to address this problem has not received much attention. Sensitive, high-resolution mid-IR observations are significantly easier to obtain than similar observations in the far-IR. The limited number of objects in our study, however, suggests that a larger sample needs to be examined to better quantify the reliability of this method. There are 348 *IRAS* PSC sources within the GRS survey region that meet the color criteria defined by Wood & Churchwell (1989) for H II regions (including the five discussed here), plus an additional 490 that meet the slightly relaxed criteria of Felli et al. (2002) for candidate H II regions. The *ISO* camera observed almost 7 deg^2 within the GRS survey region, typically at $\lambda \sim 6$ or 14 μm at 1.″5–6″ resolution, including at least 70 candidate H II regions (Felli et al. 2002). The next step in this project is to combine the

[11] For consistency, we use the observations of Testi et al. (1999), who observed all five of our cores at the same wavelength (3.6 cm) and sensitivity.

infrared observations with distances from the GRS data. This will allow us to determine the multiplicity of the embedded clusters and hence to derive the IR stellar luminosity function in the Galactic ring.

5. SUMMARY

Five dense cores selected from the ^{13}CO Galactic Ring Survey were imaged at 12.5 and 20.6 μm at 1″–2″ resolution. At scales of ~1″–20″ (0.03–0.58 pc), four of the five cores show multiple compact sources, extended structure, or both. All show extended emission on larger angular scales, ~1′–20′. In each core, the extended mid-IR emission is well correlated with the radio continuum emission from the H II regions. The correspondence between the mid-IR and radio emission and the lack of limb brightening indicate that the warm dust resides in a clumpy medium throughout the H II regions, not just in a thin shell outside the ionized gas. Dividing the radio and *IRAS* fluxes in the ratio of the 12.5 μm emission from the compact sources gives good agreement between the ZAMS spectral types needed to produce the observed radio and far-IR fluxes. In contrast, assigning all the flux to a single star results in an earlier far-IR spectral type than that from the radio data by 1–2 subclasses. Application of this method to the additional ~350–840 candidate H II regions in the GRS region will allow us to derive the IR stellar luminosity function in the Galactic ring.

We would like to thank the anonymous referee whose careful reading added to the clarity of this paper. We would like to thank the telescope operators of the IRTF for their assistance during the observations. K. E. K. would like to thank the National Research Council for support via a Research Associateship through the Air Force Office of Scientific Research. This project was supported in part by NASA grant NAG 5-10808. The Galactic Ring Survey is supported in part by NSF grants AST 98-00334 and AST 00-98562. Data from the GRS are available at http://www.bu.edu/grs. The Five College Radio Astronomy Observatory is supported in part by NSF grant AST 01-00793. This research has made use of NASA's Astrophysics Data System Abstract Service, and SIMBAD, the on-line Dictionary of Nomenclature of Celestial Objects of the CDS.

APPENDIX A

SOURCE NAMES

Table 6 summarizes the names used in other studies for the GRS sources examined here. Most names are based on Galactic coordinates, although two, IRAS and NVSS, are in B1950.0 and J2000.0 coordinates, respectively.

TABLE 6
SOURCE NAMES

		RADIO CONTINUUM[a]			
CO (GRSMC)	INFRARED (IRAS)	WC	NVSS	ZGS	TFT
45.073+0.129	19110+1045	G45.07+0.13	...	...	G045.070/072+0.132 (11/12)
45.122+0.132	19111+1048	G45.12+0.13	191327+105338	045.129+0.132	G045.123+0.132 (15)
45.190−0.438	19132+1035	...	191539+104123	...	G045.190−0.439 (34)
45.453+0.060	19120+1103	G45.45+0.06	191421+110913	045.454+0.060	G045.455+0.060/059 (18/33)
45.478+0.131	19117+1107	G45.48+0.13	191408+111229	045.477+0.130	G045.479+0.130 (32)
45.478+0.131	19117+1107	G45.48+0.13	191408+111229	045.480+0.136	G045.479+0.130 (32)

[a] WC: 2 and 6 cm (Wood & Churchwell 1989); NVSS: 21 cm (Condon et al. 1998), the "NVSS J" prefixes have been omitted from the NVSS source names; ZGS: 21 cm (Zoonematkermani et al. 1990;); TFT: 3.6 and 6 cm (Testi et al. 1999 [the number in parentheses is the source number from their Table 1]).

REFERENCES

Aumann, H. H., Fowler, J. W., & Melnyk, M. 1990, AJ, 99, 1674
Ball, R., Arens, J. F., Jernigan, J. G., Keto, E., & Meixner, M. 1992, ApJ, 389, 616
Barsony, M., Schombert, J. M., & Kis-Halas, K. 1991, ApJ, 379, 221
Chaty, S., Rodríguez, L. F., Mirabel, I. F., Geballe, T. R., Fuchs, Y., Claret, A., Cesarsky, C. J., & Cesarsky, D. 2001, A&A, 366, 1035
Churchwell, E., Wolfire, M. G., & Wood, D. O. S. 1990, ApJ, 354, 247
Cohen, M., Witteborn, F. C., Walker, R. G., Bregman, J. D., & Wooden, D. H. 1995, AJ, 110, 275
Condon, J. J., Cotton, W. D., Greisen, E. W., Yin, Q. F., Perley, R. A., Taylor, G. B., & Broderick, J. J. 1998, AJ, 115, 1693
Dudley, C. C., & Wynn-Williams, C. G. 1997, ApJ, 488, 720
Dyson, J., & Williams, D. A. 1997, The Physics of the Interstellar Medium (2d ed.; Bristol: IPP)
Emerson, J. P. 1988, in Formation and Evolution of Low-Mass Stars, ed. A. K. Dupree & M. T. V. T. Lago (NATO ASI Ser. C, 241; Dordrecht: Kluwer), 193
Feldt, M., Stecklum, B., Henning, Th., Hayward, T. L., Lehmann, Th., & Klein, R. 1998, A&A, 339, 759
Felli, M., Comoretto, G., Testi, L., Omont, A., & Schuller, F. 2000, A&A, 362, 199
Felli, M., Testi, L., Schuller, F., & Omont, A. 2002, A&A, 392, 971
Garay, G., Rodríguez, L. F., Moran, J. M., & Churchwell, E. 1993, ApJ, 418, 368
Garay, G., Rodríguez, L. F., & van Gorkom, J. H. 1986, ApJ, 309, 553
Ghosh, S. K., & Ojha, D. K. 2002, A&A, 388, 326
Hackwell, J. A., Grasdalen, G. L., & Gehrz, R. D. 1982, ApJ, 252, 250
Harvey, P. M., & Gatley, I. 1983, ApJ, 269, 613
Hayward, T. L., Miles, J. E., Houck, J. R., Gull, G. E., & Shoenwald, J. 1993, Proc. SPIE, 1946, 334
Hayward, T. L., Miles, J. W., Houck, J. R., & Timberlake, T. K. 1994, in Infrared Astronomy with Arrays: The Next Generation, ed. I. S. McLean (Dordrecht: Kluwer), 319
Helou, G., Khan, I. R., Malek, L., & Boehmer, L. 1988, ApJS, 68, 151
Hoffmann, W. F., Fazio, G. G., Shivanandan, K., Hora, J. L., & Deutsch, L. K. 1994, Infrared Phys. Tech., 35, 175
Hoffmann, W. F., Hora, J. L., Fazio, G. G., Deutsch, L. K., & Dayal, A. 1998, Proc. SPIE, 3354, 647

Hofner, P., Peterson, S., & Cesaroni, R. 1999, ApJ, 514, 899
Hunter, T. R., Phillips, T. G., & Menten, K. M. 1997, ApJ, 478, 283
IRAS Point-Source Catalog, Version 2.0. 1988, Joint *IRAS* Science Working Group (Washington, DC: GPO)
Jackson, J. M., Bania, T. M., Simon, R., Kolpak, M., Clemens, D. P., & Heyer, M. 2002, ApJ, 566, L81
Kraemer, K. E., Deutsch, L. K., Jackson, J. M., Hora, J. L., Fazio, G. G., Hoffmann, W. F., & Dayal, A. 1999, ApJ, 516, 817
Kraemer, K. E., Jackson, J. M., Deutsch, L. K., Hora, J. L., Fazio, G. G., Hoffmann, W. F., & Dayal, A. 2001, ApJ, 561, 282
Krisciunas, K., Sinton, W., Tholen, D., Tokunaga, A., Golisch, W., Griep, D., Kaminski, C., Impey, C., & Christian, C. 1987, PASP, 99, 887
Kurtz, S., Churchwell, E., & Wood, D. O. S. 1994, ApJS, 91, 659
Lada, E. A., & Lada, C. J. 1995, AJ, 109, 1682
Lada, C. J., Muench, A. A., Haisch, K. E., Jr., Lada, E. A., Alves, J. F., Tollestrup, E. V., Willner, S. P. 2000, AJ, 120, 3162
Mathis, J. S. 1990, ARA&A, 28, 37
McQuinn, K. B. W., Simon, R., Law, C. J., Jackson, J. M., Bania, T. M., Clemens, D. P., & Heyer, M. H. 2002, ApJ, 576, 274
Natta, A., & Panagia, N. 1976, A&A, 50, 191
Panagia, N. 1973, AJ, 78, 929
Rieke, G. H., Lebofsky, M. J., & Low, F. J. 1985, AJ, 90, 900
Schraml, J., & Mezger, P. G. 1969, ApJ, 156, 269
Scoville, N. Z., & Kwan, J. 1976, ApJ, 206, 718
Simon, R., Jackson, J. M., Clemens, D. P., Bania, T. M., & Heyer, M. H. 2001, ApJ, 551, 747
Simon, R., Jackson, J. M., Clemens, D. P., Bania, T. M., Kolpak, M., & Heyer, M. H. 1999, BAAS, 84.08
Straw, S. M., Hyland, A. R., & McGregor, P. J. 1989, ApJS, 69, 99
Testi, L., Felli, M., & Taylor, G. B. 1999, A&AS, 138, 71
Tokunaga, A. T. 1984, AJ, 89, 172
Tokunaga, A. T., Golisch, W. F., Griep, D. M., Kaminski, C. D., & Hanner, M. S. 1988, AJ, 96, 1971
Wood, D. O. S., & Churchwell, E. 1989, ApJS, 69, 831
Zoonematkermani, S., Helfand, D. J., Becker, R. H., White, R. L., & Perley, R. A. 1990, ApJS, 74, 181